nature communications

Article

https://doi.org/10.1038/s41467-025-60919-7

Planar asymmetric surface $Fe^{IV}=O$ synthesis with pyrite and chlorite for efficient oxygen atom transfer reactions

Received: 3 January 2025

Accepted: 5 June 2025

Published online: 01 July 2025

Check for updates

Wengao Lian[1,3], Hengyue Xu[2,3], Xingyue Zou[1,3], Jie Dai[1], Meiqi Li[1], Cancan Ling[1], Yunhao Shen[1], Hao Li[1], Yancai Yao[1] ✉ & Lizhi Zhang[1] ✉

Surface high-valent iron-oxo species (≡Fe^{IV}=O) are reliable and green oxygen atom transfer reagents, but the ability is seriously inhibited by the maximal orbital overlap of axial Fe = O double bond in a symmetric planar coordination environment. Herein, we report the synthesis of planar asymmetric surface Fe^{IV} = O (PA-≡Fe^{IV} = O) on pyrite using chlorite as the oxidant, where the in-situ generated ClO_2 can transform a planar Fe-S bond to Fe-Cl by oxidizing and subsequently substituting planar sulfur atoms. Different from planar symmetric surface Fe^{IV} = O (PS-≡Fe^{IV} = O) with electron localization around axial Fe = O, PA-≡Fe^{IV} = O delocalizes electrons among Fe, axial oxo moiety and its planar ligands owing to the stronger electron-withdrawing capacity of Cl, which effectively weakens the orbital overlap of axial Fe = O bonding and thus facilitates the rapid electron transfer from the substrates to the unoccupied antibonding orbital of PA-≡Fe^{IV} = O, realizing more efficient oxygen atom transfer oxidation of methane, methyl phenyl sulfide, triphenylphosphonate and styrene than PS-≡Fe^{IV} = O. This study offers a facile approach for the synthesis of planar asymmetric surface Fe^{IV} = O, and also underscores the importance of planar coordination environment of high-valent metal-oxo species in the oxygen atom transfer reactions.

High-valent iron-oxo species (Fe^{IV}=O) are prevalent in metalloenzymes such as Rieske dioxygenase, cytochrome P450, playing a crucial role in various naturally biological processes for the selective C–H or C = C bond activation during the metabolites synthesis and xenobiotic degradation[1–4]. These metalloenzyme-catalyzed processes involve the formation of Fe^{IV} = O with a low-lying unoccupied antibonding orbital, which effectively transfer its axial oxo moiety to substrates with unpaired electrons[5–7]. These processes have inspired many metalloenzymes-like chemical syntheses via oxygen atom transfer of artificial Fe^{IV} = O, strongly depending on the efficient synthesis of highly active Fe^{IV} = O species. Although great efforts have been made in the synthesis of homogeneous Fe^{IV} = O species through mimicking the enzymatic iron centers, their fragile organic ligands disfavor the robust catalysis in an oxidized environment[8–10], and their homogeneous nature also increases the difficulty in separation. Recently, well-tailored iron carriers, such as zero-valent iron (nZVI) and iron-based zeolites[11,12], have been employed to synthesize surface Fe^{IV} = O species (≡Fe^{IV}=O) coordinated with simple inorganic ligands by using common oxidants (e.g., perhydrol, persulfate, peracetic acid) as the oxygen source[13–15]. Generally, these robust and heterogonous ≡Fe^{IV} = O possess an octahedral structure with four planar symmetric ligands in an Fe-O_4 configuration, whose localized electron distribution results in their strong "acceptance–backdonation" interactions between the 3*d* orbitals of Fe and the 2*p* orbitals of axial oxo, preventing ≡Fe^{IV} = O from accepting

[1]State Key Laboratory of Green Papermaking and Resource Recycling, National observation and Research Station of Erhai Lake Ecosystem in Yunnan, Yunnan Dali Research Institute, School of Environmental Science and Engineering, Shanghai Jiao Tong University, Shanghai, P. R. China. [2]Department of Chemistry, Tsinghua University, Beijing, P. R. China. [3]These authors contributed equally: Wengao Lian, Hengyue Xu, Xingyue Zou. ✉e-mail: yyancai@sjtu.edu.cn; zhanglizhi@sjtu.edu.cn

electrons from substrates and thus slowing the subsequent oxygen atom transfer processes[16].

This localized electron distribution around the axial Fe = O bond might be destroyed by breaking its planar symmetric coordination structure via substituting one or more planar atoms with more electronegative ones, which can weaken the strength of axial ligand through the electron transfer from the axial bond to the planar one[17]. In theory, this electron redistribution can build a strong local electric field around the central metal atom to enhance the electron delocalization around axial Fe = O bond, thus favoring the electron transfer process from the substrates to the central metal atom[18,19], which was recently verified by the more efficient reduction of uranyl(VI) to uranium(IV) after partial removal of planar Cl ligand to disrupt the symmetry of planar atomic structure[20].

Pyrite (FeS_2), characterized by abundant surface ≡Fe^{II} sites and easily-substituted planar S ligands, is more suitable for planar asymmetric ≡Fe^{IV} = O synthesis than commonly-used iron carriers of strong Fe-O bonds[21–24]. Chlorite (ClO_2^-), with decent oxidation capacity, safe storage and less environmental risks than other oxidants (e.g., H_2O_2 and Peroxymonosulfate), is found to be a desirable oxidant in ≡Fe^{IV} = O synthesis with high selectivity[11]. In this study, we demonstrate the synthesis of planar asymmetric ≡Fe^{IV} = O with FeS_2 and chlorite, given their reaction can simultaneously produce ≡Fe^{IV} = O on the surface of FeS_2 and chlorine dioxide (ClO_2)[25,26], while the in-situ generated ClO_2 might oxidize the planar coordinated sulfur atoms of symmetric ≡Fe^{IV} = O to substitute S by Cl[27]. The synthesis process was carefully checked by the Extended X-ray absorption fine structure (EXAFS), Mössbauer spectroscopy, and in-situ Raman spectra. The electrophilicity of axial Fe = O bond and its OAT performance were subsequently investigated with theoretical calculations, including electron spin density, electron localization function (ELF), density of states (DOS), and transfer energy barrier of oxygen atoms. Finally, planar asymmetric ≡Fe^{IV} = O was employed to trigger OAT reactions such as selective methane (CH_4) conversion to methanol (CH_3OH), triphenylphosphonate oxidation and styrene epoxidation, showcasing its potential for selective oxidation.

Results

Synthesis and characterization

The Fe-S coordination environment coupled with abundant surface Fe^{II} sites (≡Fe^{II}) on FeS_2, as revealed by transmission electron microscopy, elemental mapping, Raman spectroscopy, and X-ray photoelectron spectroscopy (XPS), favors the construction of PS-≡Fe^{IV} = O on FeS_2 (Supplementary Figs. 1–3). First, we employed in-situ surface-enhanced Raman spectroscopy to investigate the molecular processes associated with ClO_2^- dissociation and subsequent PS-≡Fe^{IV} = O formation. The introduction of ClO_2^- into the FeS_2-containing solution immediately resulted in the emergence and gradual increase of a characteristic Raman peak of the δ(H···Cl–O) bending mode (387.5 cm^{-1}), suggesting that the terminal O of ClO_2^- could interact with neighboring H_2O molecules to form hydrogen bonds (H···Cl–O), thereby significantly stretching the Cl–O bond for its subsequent cleavage[11] (Fig. 1a). Along with the oxygen atom transfer from ClO_2^- to ≡Fe^{II} sites of FeS_2, PS-≡Fe^{IV} = O was then formed in an octahedral structure with a planar symmetric Fe-S_4 configuration, as reflected by the enhanced Raman peak at 920.7 cm^{-1} (Eq. 1, Fig. 1a and Supplementary Figs. 4 and 5) and the presence of a seven-split signal in electron paramagnetic resonance (EPR) spectra using 5,5-dimethyl-1-pyrrolidine-N-oxide (DMPO) as the spin-trapping agent[28] (Supplementary Fig. 6). The appearance of four peaks with the same 17 G interval in the EPR spectra indicated the simultaneous generation of ClO_2 during the PS-≡Fe^{IV} = O formation[29] (Fig. 1b), which was supported by the increasing absorbance of ClO_2 at 350 nm along with the decreasing absorbance of ClO_2^- at 262 nm, indicative of the conversion of ClO_2^- to ClO_2 (Fig. 1c). Regarding that ClO_2 can be generated through two possible pathways including the activation of ClO_2^- via the electron transfer from ClO_2^- to ≡Fe^{IV} = O (Eq. 2) and the direct disproportionation of ClO_2^-[26,30] (Eq. 3 and Supplementary Figs. 7 and 8), we then quantified the production of ClO_2 by quenching ≡Fe^{IV} = O with dimethyl sulfoxide (DMSO), and found that the ClO_2 generation rate was only reduced by ~10% (Supplementary Figs. 9 and 10), suggesting that ClO_2 was mainly generated through the disproportionation of ClO_2^- and thereby ensuring the coexistence of PS-≡Fe^{IV} = O and ClO_2 for subsequent PA-≡Fe^{IV} = O synthesis.

$$\equiv Fe^{II} + ClO_2^- \rightarrow \equiv Fe^{IV} = O + ClO^- \quad (1)$$

$$\equiv Fe^{IV} = O + ClO_2^- \rightarrow \equiv Fe^{III} + ClO_2 \quad (2)$$

$$H^+ + ClO_2^- \rightarrow Cl^- + ClO_2 \quad (3)$$

We interestingly found that the amount of chlorine-containing species in solution decreased from 1.0 mmol L^{-1} to 0.92 mmol L^{-1} after 2 h of reaction, indicative of partial chlorine binding onto the FeS_2 surface (Supplementary Figs. 11–13). To deeply understand this process, we quenched ClO_2 with sodium thiosulfate ($Na_2S_2O_3$) or ascorbic acid ($C_6H_8O_6$) utilizing their easy oxidation by ClO_2 and slow reaction with ClO_2^-, and observed a sharp increase of SO_4^{2-} concentration in the presence of ClO_2, owing to the oxidation of some planar coordinated S atoms in PS-≡Fe^{IV} = O into aqueous SO_4^{2-} by ClO_2 (Eq. 4 and Supplementary Figs. 14–18). Subsequently, ^{34}S isotope labeling further confirmed ClO_2^- induced S oxidation in FeS_2 (Supplementary Fig. 19). In-situ attenuated total reflectance Fourier transform infrared spectrometer (ATR-FTIR) analysis displayed a left-shifted SO_4^{2-} peak (1089 cm^{-1} for $Fe^{34}S_2$ compared to 1106 cm^{-1} for $Fe^{32}S_2$) upon ClO_2 exposure, with signal disappearance post-ClO_2 quenching, verifying FeS_2 as the S source and underscoring the critical role of ClO_2 (Supplementary Fig. 20). Aligning well with these findings, inductively coupled plasma-Mass Spectrometry detected 3.15 mg L^{-1} ^{34}S and 2.85 mg L^{-1} ^{32}S with ClO_2, but negligible sulfur signals without ClO_2 (Supplementary Fig. 21). Meanwhile, the appearance of a strong XPS signal of Fe-Cl bonds at 198.5 eV for the FeS_2 reacted with ClO_2 (R-FeS_2-ClO_2), was in sharp contrast to the ignorable signals of Fe-Cl bonds on the reacted FeS_2 (R-FeS_2) when ClO_2 was quenched (Fig. 1d and Supplementary Fig. 22). Moreover, Raman shifts at 212 cm^{-1} and 279 cm^{-1} further evidenced the formation of Fe-Cl bonds on the R-FeS_2-ClO_2, different from the observed Fe-S bonds on the R-FeS_2 (Fig. 1e and Supplementary Fig. 23).

$$Fe - S + ClO_2 + H_2O \rightarrow Fe - Cl + SO_4^{2-} + H^+ \quad (4)$$

We then checked the role of other Cl species (i.e., ClO_2^- and Cl^-) in the synthesis of PA-≡Fe^{IV} = O. The Cl atom with a higher electrophilicity (0.855) in ClO_2 was more positively charged than that of ClO_2^- (−0.153), and thus more powerful to oxidize the negatively charged S atom (Supplementary Figs. 24 and 25 and Supplementary Tables 1 and 2), consistent with the significantly lower LUMO orbital energy of ClO_2 than that of ClO_2^- (Supplementary Figs. 26 and 27). The contribution of Cl^- was excluded by the negligible Raman signal of Fe-Cl bonds on FeS_2 reacted with Cl^- for 2 h (Supplementary Fig. 28). Consequently, we conclude that ClO_2 plays a crucial role in transforming the planar Fe-S bond in PS-≡Fe^{IV} = O to the Fe-Cl one and distorting the original symmetric Fe-S_4 configuration, rather than ClO_2^- and Cl^-.

Coordination and electronic structures

We thereafter characterized the coordination structures of PA-≡Fe^{IV} = O and PS-≡Fe^{IV} = O with the Fe K-edge EXAFS spectra and the wavelet transformation contour plots (Fig. 1f, g and Supplementary

https://doi.org/10.1038/s41467-025-60919-7

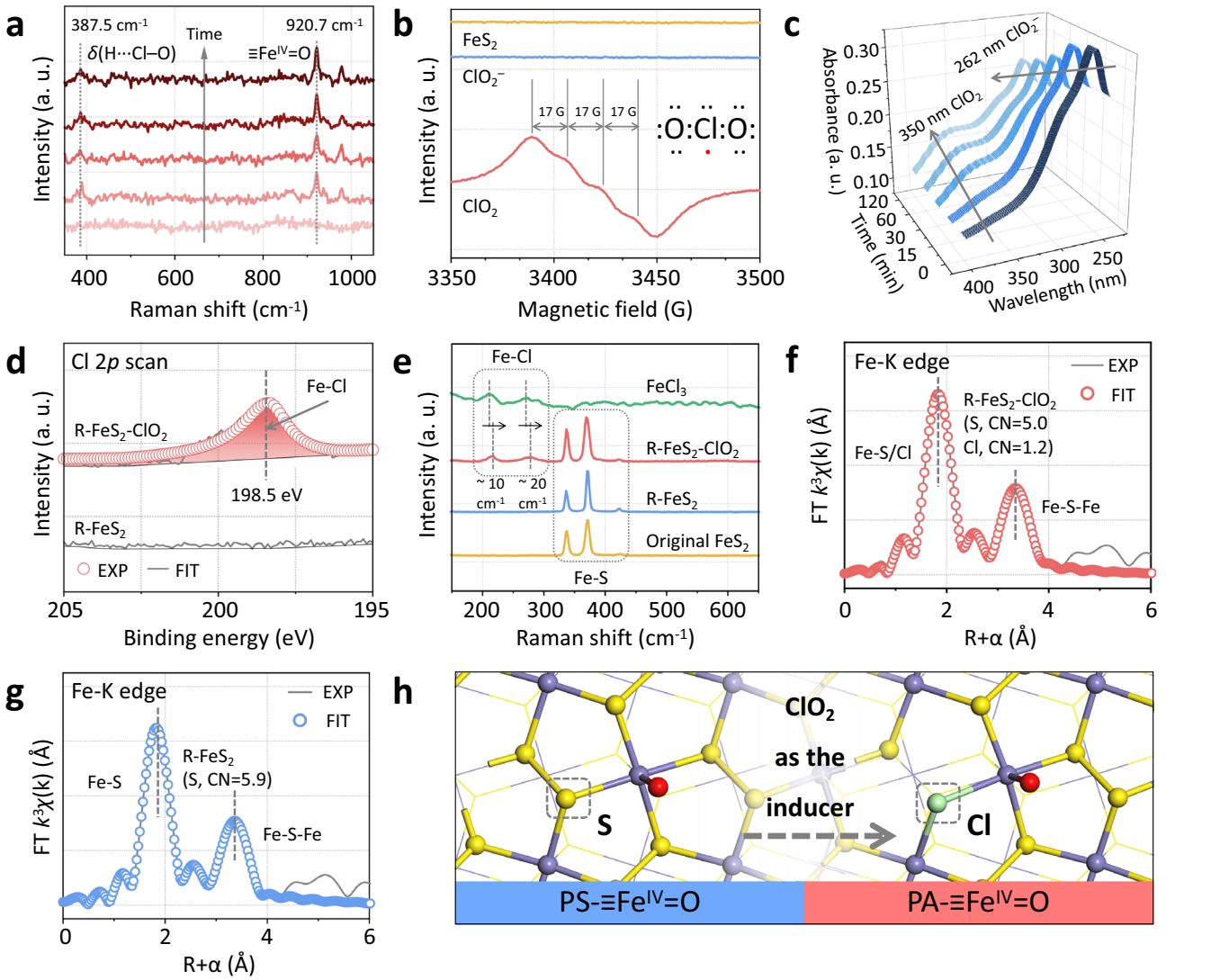

Fig. 1 | Synthesis and characterization of PA-≡Fe^{IV} = O. a In-situ Raman spectra to investigate the formation of δ(H···Cl–O) and the generation process of ≡Fe^{IV} = O with FeS_2 and ClO_2^-. **b** EPR spectra to determine ClO_2 generated by FeS_2 and ClO_2^- without any trapping agent. **c** UV–vis spectra to detect the transformation from ClO_2^- (262 nm) to ClO_2 (350 nm). **d** XPS spectra of Cl 2*p* scan on R-FeS_2-ClO_2 and R-FeS_2. **e** Raman spectra of the Fe-Cl bond and Fe-S bond signals in R-FeS_2-ClO_2, R-FeS_2, original FeS_2 and $FeCl_3$. EXAFS spectra and corresponding fitting lines of (**f**) R-FeS_2-ClO_2 and **g** R-FeS_2. **h** Illustration of the transformation process from Fe-S to Fe-Cl bond for PA-≡Fe^{IV} = O synthesis with ClO_2 as the inducer. The blue ball refers to the Fe atom, the yellow ball refers to the S atom, the green ball refers to the Cl atom and the red ball refers to the O atom. **Experiment conditions**: $[FeS_2]_0$ = 1.0 g/L (if not specified), $[ClO_2^-]_0$ = 1.0 mmol/L (if not specified), $[Na_2S_2O_3]_0$ = 1.0 mmol/L (if not specified).

Fig. 29). In the fitted EXAFS spectra, the coordination numbers of Cl and S in the first shell of Fe in R-FeS_2-ClO_2 were calculated to be 1.2 ± 0.1 and 5.0 ± 0.1 respectively. In contrast, only a coordination number of 5.9 ± 0.1 was determined for S in the R-FeS_2 (Supplementary Table 3). These fitting results suggested that one of the four planar Fe-S bonds in PS-≡Fe^{IV} = O was transformed to the Fe-Cl bond, generating a planar asymmetric Fe-Cl_1S_3 configuration in PA-≡Fe^{IV} = O (Fig. 1h, Supplementary Figs. 30–36 and Supplementary Table 4). Different from the planar symmetric Fe-S_4 configuration with uniform electron distribution, this planar asymmetric Fe-Cl_1S_3 configuration might disrupt the original electron structure due to the stronger electron-withdrawing ability of Cl, as evidenced by the electrostatic potential analysis of more negatively charged Cl (Fig. 2a). Therefore, we investigated the electronic structures of PA-≡Fe^{IV} = O and PS-≡Fe^{IV} = O, and found that the Fe K-edge X-ray absorption near edge structure (XANES) spectra of R-FeS_2-ClO_2 experienced a right-shift of ~0.2 eV in comparison with pristine FeS_2 and R-FeS_2, indicative of a slightly increased Fe valence state in PA-≡Fe^{IV} = O (Fig. 2b and Supplementary Fig. 37), as supported by the left-shift in the Fe 2*p* XPS of R-FeS_2-ClO_2[31,32] (Fig. 2c). To further clarify the differences of electronic properties between PA-≡Fe^{IV} = O and PS-≡Fe^{IV} = O, we measured their ^{57}Fe Mössbauer spectra, where the isomer shift (δ) reflects the electron density around the ^{57}Fe nucleus in PA-≡Fe^{IV} = O or PS-≡Fe^{IV} = O[33] (Supplementary Table 5 and Supplementary Fig. 38). Although the fitted parameters suggested both PS-≡Fe^{IV} = O and PA-≡Fe^{IV} = O possessed the high valence state and high spin state (S = 2), the δ value (0.05 mm s^{-1}) in the doublet of PA-≡Fe^{IV} = O was much smaller than that of PS-≡Fe^{IV} = O (0.08 mm s^{-1}), confirming the decreased electron density around the Fe center of PA-≡Fe^{IV} = O (Fig. 2d), because Fe atom of PA-≡Fe^{IV} = O transferred more electrons to its ligands due to the higher electronegativity of Cl (χ = 3.16) than that of S (χ = 2.58)[34–36] (Fig. 2a), as revealed by the higher work function of PA-≡Fe^{IV} = O (4.744 eV) than that of the PS-≡Fe^{IV} = O (4.695 eV) (Fig. 2e). This transfer of more electrons from Fe center to adjacent ligands led to the downshift of the Fermi level of Fe^{IV} = O in PA-≡Fe^{IV} = O, which might facilitate its acceptance of electrons from substrates to boost the oxygen atom transfer process.

https://doi.org/10.1038/s41467-025-60919-7

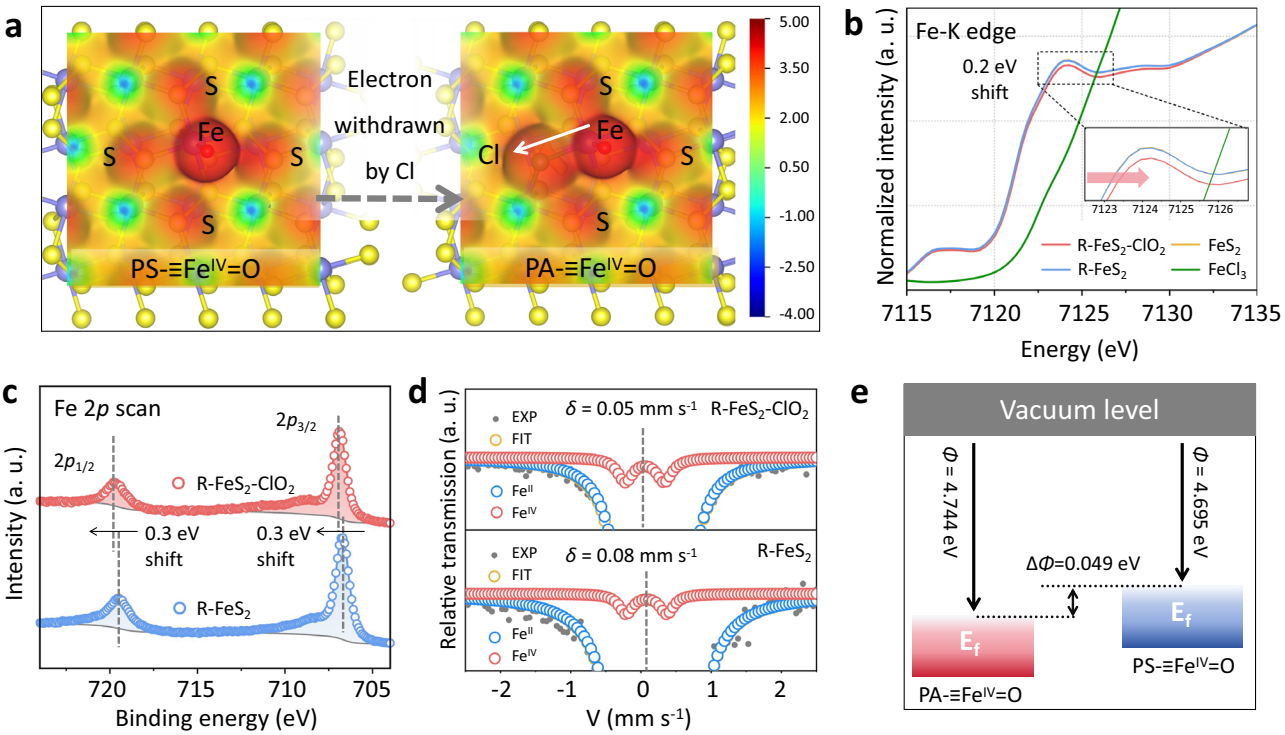

Fig. 2 | Comparison of coordination and electronic structures between PA-≡Fe^{IV}=O and PS-≡Fe^{IV}=O. a Electrostatic potential in Fe, O, S, and Cl atoms in PA-≡Fe^{IV}=O and PS-≡Fe^{IV}=O. The blue ball refers to the Fe atom, the yellow ball refers to the S atom, the green ball refers to the Cl atom and the red ball refers to the O atom. **b** Fe K-edge XANES spectra of R-FeS$_2$-ClO$_2$, R-FeS$_2$, original FeS$_2$ and FeCl$_3$. **c** XPS spectra on Fe 2*p* scan of R-FeS$_2$-ClO$_2$ and R-FeS$_2$. **d** Mössbauer spectra to differentiate the electronic structure of PA-≡Fe^{IV}=O and PS-≡Fe^{IV}=O. **e** Schematic illustration of the work functions of PA-≡Fe^{IV}=O and PS-≡Fe^{IV}=O. E_f represents the Fermi level. **Experiment conditions**: $[FeS_2]_0$ = 1.0 g/L (if not specified), $[ClO_2^-]_0$ = 1.0 mmol/L (if not specified), $[Na_2S_2O_3]_0$ = 1.0 mmol/L (if not specified).

Theoretical investigations

We thus carried out theoretical calculations to further investigate the oxygen atom transfer capacity of PA-≡Fe^{IV}=O and PS-≡Fe^{IV}=O. When one planar S atom in PS-≡Fe^{IV}=O was replaced by Cl, the originally localized electrons around the axial Fe=O were induced to redistribute among the adjacent ligand atoms, which significantly enhanced the electron spin density of the ligand atoms surrounding the axial Fe=O in PA-≡Fe^{IV}=O, despite negligible changes in the electron spin state of Fe itself (Fig. 3a). In this case, the delocalized electrons around PA-≡Fe^{IV}=O facilitated the electron transfer across different atoms, thus enhancing oxygen atom transfer process. To further elucidate the enhanced electron-withdrawing and the corresponding oxygen atom transfer processes in PA-≡Fe^{IV}=O, we then analyzed the ELF cross-sections near the Fe atom and its ligands, and found that the Fe and O atoms in PA-≡Fe^{IV}=O respectively carried a more positive charge of +1.829 e and a more negative charge of −0.820 e than those of PS-≡Fe^{IV}=O (+1.264 e, and −0.699 e)[37–39] (Fig. 3b). Obviously, this greater electronic delocalization and stronger ionic characteristic significantly weakened the axial Fe=O bond in PA-≡Fe^{IV}=O, as reflected by the lower oxygen release energy barriers of PA-≡Fe^{IV}=O (0.156 eV and 3.25 eV) than PS-≡Fe^{IV}=O (0.576 eV and 3.41 eV) in the two electron transfer steps of oxygen transfer process (Fig. 3c). The calculated delocalization in Fe=O bond and the lowered oxygen transfer energy barrier were further corroborated by in-situ Raman spectroscopy. The progressive right-shift of the Fe=O stretching frequency from 920.7 cm^{-1} (PS-≡Fe^{IV}=O) to 929.2 cm^{-1} (PA-≡Fe^{IV}=O) directly reflected the weakening of the Fe=O bond due to electron delocalization (Supplementary Fig. 39). Furthermore, DOS analysis revealed distinct electronic configurations between PA-≡Fe^{IV}=O and PS-≡Fe^{IV}=O (Fig. 3d, e). PA-≡Fe^{IV}=O exhibited continuous Fe states near the Fermi level, indicating enhanced electron delocalization along Fe=O, which reduced the bandgap and facilitated efficient electron transfer. In contrast, PS-≡Fe^{IV}=O possessed more discrete states with a larger bandgap, reflecting localized electrons and lower reactivity. This divergence stemmed from ligand field effects that stronger electronic confinement in PS-≡Fe^{IV}=O stabilized uniform electron distribution, which is unfavorable for delocalization. Overall, the planar asymmetric structure of PA-≡Fe^{IV}=O could delocalize and weaken its axial Fe=O bond to enhance its oxygen atom transfer ability.

Oxygen atom transfer reactions

We first chose oxidation of CH_4 to investigate the influence of planar coordination environment on the oxygen atom transfer efficiency of ≡Fe^{IV}=O species, regarding that direct CH_4 oxidation to CH_3OH offers a promising route to access various fundamental feedstocks for the chemical industry, but the high C−H dissociation energy (~439 kJ mol^{-1}) and the robust non-polar structure of CH_4 significantly challenges its efficient and selective conversion[40–42]. Although CH_4 can be exclusively oxidized to CH_3OH by ≡Fe^{IV}=O under ambient conditions, the sluggish oxygen transfer of transitional ≡Fe^{IV}=O resulted in low CH_3OH yield rate[43,44]. As expected, with a selectivity exceeding 95%, the PA-≡Fe^{IV}=O could efficiently oxidize CH_4 to CH_3OH with a yield rate of 312.67 μmol h^{-1} g_{pyrite}^{-1}, far superior to the PS-≡Fe^{IV}=O counterpart (188.42 μmol h^{-1} g_{pyrite}^{-1}) (Fig. 4a and Supplementary Figs. 40–42) as well as most records of traditional methods including light irradiation, heating, pressurizing and multiple combined one (Fig. 4b and Supplementary Table 6). Under the same reaction conditions, CH_3OH was not detected during the control experiments with using FeS_2, ClO_2^- or ClO_2 alone, demonstrating the indispensable contribution of ≡Fe^{IV}=O to the CH_4 oxidation (Supplementary Fig. 40).

To give deep insights into the superior oxygen atom transfer performance of PA-≡Fe^{IV}=O, we then investigated the mechanism of

https://doi.org/10.1038/s41467-025-60919-7

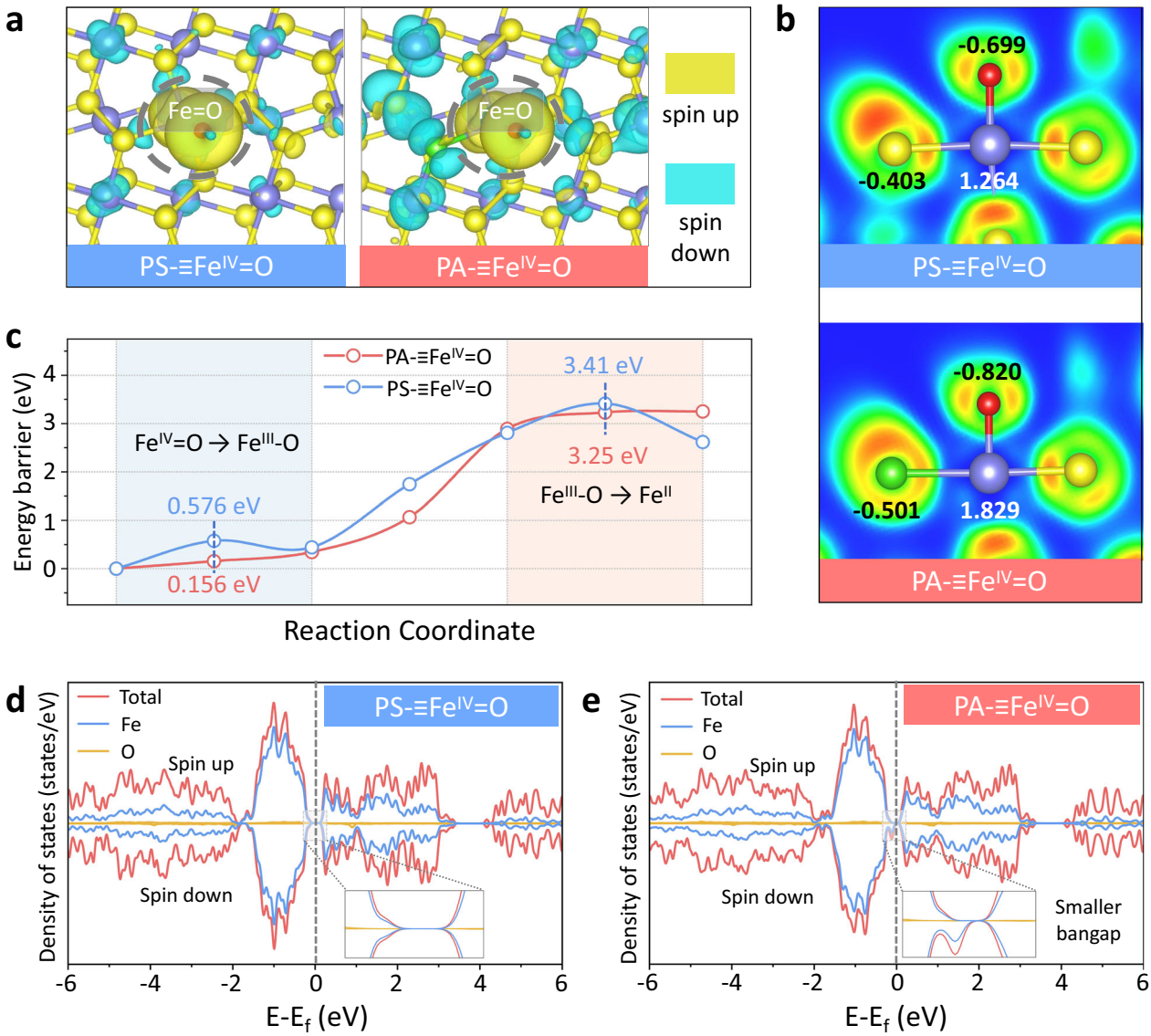

Fig. 3 | Theoretical analysis on the enhanced oxygen atom transfer capacity of PA-≡Fe^{IV}=O. a Comparison of electron spin density between PA-≡Fe^{IV}=O and PS-≡Fe^{IV}=O. **b** Electron localization function (ELF) analysis of PA-≡Fe^{IV}=O and PS-≡Fe^{IV}=O. The blue ball refers to Fe atom, the yellow ball refers to S atom, the green ball refers to Cl atom and the red ball refers to the O atom. **c** Differences of oxygen atom transfer energy barrier in the two steps between PA-≡Fe^{IV}=O and PS-≡Fe^{IV}=O. **d** Density of states analysis on PS-≡Fe^{IV}=O. **e** Density of states analysis on PA-≡Fe^{IV}=O.

selective CH_4 oxidation at the molecular scale. As illustrated by the widely accepted CH_4 oxidation mechanism mediated by ≡Fe^{IV}=O (Fig. 4c), the C–H bond of CH_4 is significantly stretched upon its adsorption onto ≡Fe^{IV}=O site, leading to its cleavage into a crucial radical intermediate (•CH_3), along with the formation of ≡Fe^{III}–OH through an H-abstraction process (Supplementary Figs. 43 and 44)[45,46]. Given that the formation of •CH_3 is regarded as the rate-determining step for the CH_4 oxidation, we thus carried out EPR experiments with DMPO as a spin-trapping agent to dynamically monitor the generation of •CH_3 in the CH_4-saturated aqueous solutions with PA-≡Fe^{IV}=O and PS-≡Fe^{IV}=O. As expected, a stronger DMPO–•CH_3 signal was detected in the PA-≡Fe^{IV}=O system (Fig. 4d and Supplementary Fig. 45), verifying the enhanced electron-accepting ability of PA-≡Fe^{IV}=O, and also consistent with the results of XPS and Mössbauer spectra as well as the corresponding theoretical calculations. This •CH_3 then captures the axial OH of ≡Fe^{III}–OH via an oxygen-rebound step for the selective CH_3OH formation rather than the C–C couple to generate CH_3-CH_3 as a result of the strong adsorption interactions between •CH_3 and ≡Fe^{III}–OH (Supplementary Fig. 46). The enhanced oxygen transfer ability of PA-≡Fe^{IV}=O was further confirmed by the stronger C–O bonds vibrations of CH_3OH in the in-situ ATR-FTIR spectra with PA-≡Fe^{IV}=O, accounting for its higher CH_3OH yields (Fig. 4e and Supplementary Fig. 47), as evidenced by the much lower transition state energy barrier (0.205 eV) of PA-≡Fe^{IV}=O than that of PS-≡Fe^{IV}=O (1.050 eV) (Fig. 4f).

Besides selective CH_4 oxidation, PA-≡Fe^{IV}=O exhibited better oxygen atom transfer performance than PS-≡Fe^{IV}=O for methyl phenyl sulfide (MPS) oxidation, triphenylphosphine (Ph_3P) oxidation and styrene epoxidation. The MPS to MPSO oxidation rate of PA-≡Fe^{IV}=O reached 0.30 mmol L^{-1} h^{-1} (Fig. 4g and Supplementary Fig. 48), much higher than that of PS-≡Fe^{IV}=O (~ 0.18 mmol L^{-1} h^{-1}). Impressively, PA-≡Fe^{IV}=O stoichiometrically converted 0.5 mmol L^{-1} Ph_3P to triphenylphosphine oxide (Ph_3PO) in 120 min with an impressive conversion rate of 97.5%, which was merely ~70% for PS-≡Fe^{IV}=O (Fig. 4h and Supplementary Fig. 48). Furthermore, PA-≡Fe^{IV}=O enabled the epoxidation of styrene to value-added styrene oxide with a yield rate of

https://doi.org/10.1038/s41467-025-60919-7

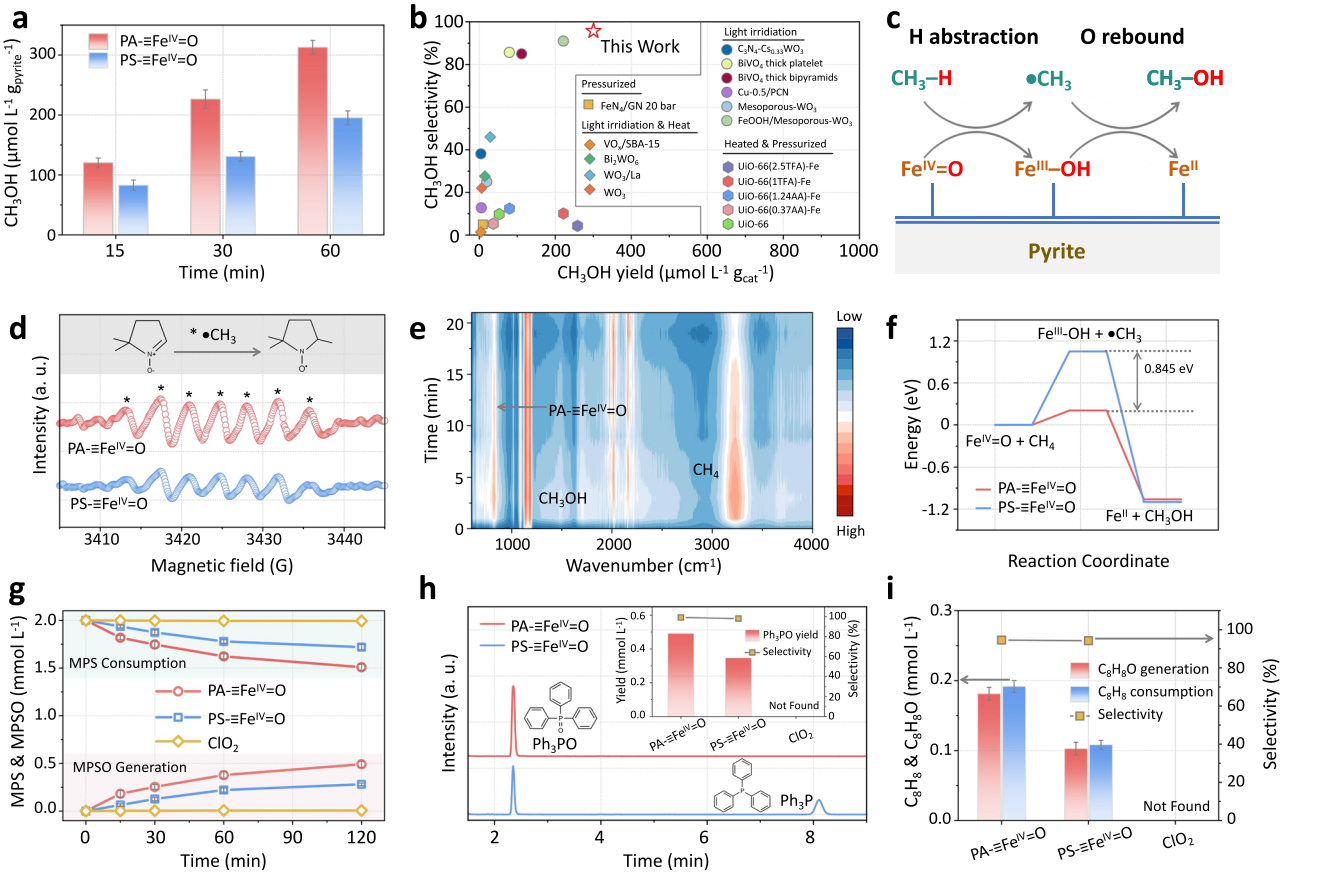

Fig. 4 | Oxygen atom transfer reactions. a Comparison of CH_3OH yield by PA-≡Fe^{IV} = O and PS-≡Fe^{IV} = O. **b** Comparison of CH_3OH yield rates in this PA-≡Fe^{IV} = O driven system with those in light- or thermal-driven CH_4 activation systems. **c** Illustration of CH_4 oxidation process by ≡Fe^{IV} = O. **d** EPR spectra to identify the ·CH_3 intermediate after H abstraction by PA-≡Fe^{IV} = O and PS-≡Fe^{IV} = O. **e** CH_4 consumption and CH_3OH generation by PA-≡Fe^{IV} = O through in-situ Fourier Transform infrared spectroscopy. **f** Energy barriers of CH_4 conversion process by PA-≡Fe^{IV} = O and PS-≡Fe^{IV} = O. **g** MPS and **h** Ph_3P oxidation efficiencies by PA-≡Fe^{IV} = O and PS-≡Fe^{IV} = O in comparison. **i** Comparison of efficiencies over PA-≡Fe^{IV} = O and PS-≡Fe^{IV} = O for styrene epoxidation to styrene oxide. **Experiment conditions**: $[FeS_2]_0$ = 0.02 g (for CH_4 oxidation), $[FeS_2]_0$ = 0.1 g (for other reactions), $[ClO_2^-]_0$ = 1.0 mmol L^{-1} (if not specified), aqueous CH_4-containing solution volume = 20 mL, other solution volume = 100 mL. The error bars represent the standard deviation derived from two repeated experiments.

0.18 mmol L^{-1} h^{-1}, much better than PS-≡Fe^{IV} = O (0.10 mmol L^{-1} h^{-1}) (Fig. 4i and Supplementary Fig. 48). Promisingly, the efficiencies of MPS, Ph_3P and styrene oxidation by PA-≡Fe^{IV} = O surpassed many previous reports, indicating the prominent advantages of PA-≡Fe^{IV} = O in selective oxidation reactions (Supplementary Table 7). These results showcase the great potential of PA-≡Fe^{IV} = O on selective synthesis of various value-added chemicals via a feasible oxygen atom transfer process.

Discussion

In conclusion, we have demonstrated the synthesis of planar asymmetric ≡Fe^{IV} = O confined on pyrite with chlorite as the oxidant, where the concomitant ClO_2 was able to oxidize a planar Fe-S bond of ≡Fe^{IV} = O to Fe-Cl, along with conversion of planar symmetric Fe-S_4 configuration into planar asymmetric Fe-Cl_1S_3 counterpart, as substantiated by various spectroscopic techniques including XAFS, Mössbauer and XPS spectra. Theoretical calculations revealed that the planar asymmetry structure formation delocalized the electron distribution around ≡Fe^{IV} = O because of the stronger electron-withdrawing capacity of Cl, and then weakened the orbital overlapping of axial Fe = O bond, thus reducing the oxygen atom transfer energy barrier and facilitating the electron transfer from substrates to PA-≡Fe^{IV} = O. This novel PA-≡Fe^{IV} = O possessed superior reactivity towards selective methane oxidation, styrene epoxidation, and sulfides/phosphides oxidation, showcasing high potential for efficient high-valued chemical production via its superior oxygen transfer ability.

Methods

Chemicals

Chemicals purchased for this research were of at least analytical grade without further operation and the information of them was listed in Supplementary Method 1.

Experimental procedures

The PA-≡Fe^{IV} = O synthesis with FeS_2 and ClO_2^- was carried out in 100-mL conical flasks in a shaker (180 rpm) under ambient pressure and at room temperature (25 °C) (Supplementary Fig. 49). To start the reaction, FeS_2 (1.0 g L^{-1}) and ClO_2^- (0.1 to 1.0 mmol L^{-1}) were introduced into the flask with 100 mL deionized water. In the quenching tests, 10.0 mmol L^{-1} DMSO or 1.0 mmol L^{-1} $Na_2S_2O_3$ was first mixed with the deionized water before reaction. The reacted FeS_2 underwent three steps of filtration, freeze-drying, and vacuum preservation for characterizations including Raman, XPS, and XAFS. (Supplementary Method 2).

CH_4-to-CH_3OH conversion experiments were conducted in a well-designed reactor (300 mL, Supplementary Fig. 50). Initially, the reactor was charged with 20 mg of FeS_2, then it was sealed and purged with

CH_4 gas (containing 2%, Ar as a balance gas) for a duration fof 30 min to purge out the air and make CH_4 saturated in the reactor. Subsequently, the deionized water saturated with CH_4 (purged with CH_4 for 30 min) was introduced into the reactor and combined with FeS_2. To trigger the reaction, ClO_2^- was injected into the reactor, followed by placing the reactor in a shaker operating at 60 rpm. This rotating speed was selected to endure the sufficient contact between CH_4 and $\equiv Fe^{IV}=O$ while prevent destroying the adsorption of C–H bond on the $\equiv Fe^{IV}=O$. Of note, all reactions were conducted at room temperature (25 °C). For the experiment for PS-$\equiv Fe^{IV}=O$ induced CH_4 oxidation, scavenger of ClO_2 was added into the solution before ClO_2^-. MPS and Ph_3P oxidation and styrene epoxidation experiments were performed in 100-mL conical flasks in a shaker (180 rpm) with FeS_2 and ClO_2^- dosed in sequence.

Analytical methods and spectroscopic characterizations

The transformation from ClO_2^- to ClO_2 was verified by the UV–vis spectrophotometer (UV-2550, Shimadzu, Japan). The quantification of ClO_2 was realized through a DPD UV–vis method (UV-2550, Shimadzu, Japan, Supplementary Method 3). Except for ClO_2, the concentrations of chlorine-containing species were detected by high-performance ion chromatography (Dionex ICS-900, Thermo). $\equiv Fe^{IV}=O$ and $\bullet CH_3$ were captured by EPR (Bruker EMXnano, German, Supplementary Method 4) with DMPO as the trapping agent. The spin state and electronic structure of PA-$\equiv Fe^{IV}=O$ and PS-$\equiv Fe^{IV}=O$ were recognized and compared by ^{57}Fe Mössbauer measurements (Wissel MS-500, Germany, Supplementary Method 5). The concentrations of MPS, Ph_3P, styrene and their corresponding oxidation products were detected using high-performance liquid chromatography (Dionex Ultimate 3000, Thermo, USA, Supplementary Method 6). The methane-to-methanol conversion rates were examined by gas chromatography (GC) equipped with a GC capillary column (30 m × 0.32 mm × 0.5 μm) and a flame ionization detector. The generation of $\equiv Fe^{IV}=O$ from FeS_2 and ClO_2^- was checked by in-situ surface enhanced Raman spectroscopy (Renishaw inVia Qontor, UK, Supplementary Method 7). The signals of CH_4 consumption and CH_3OH generation by PA-$\equiv Fe^{IV}=O$ or PS-$\equiv Fe^{IV}=O$ were recorded through in-situ ATR-FTIR (Nicolet iS50, Thermo, USA, Supplementary Method 8).

Theoretical calculations

The theoretical calculations were carried out using Vienna Ab initio Simulation Package and Gaussian 09 software based on the DFT (Supplementary Method 9).

Data availability

All study data are included in the article and Supplementary Information. Further information can be acquired from the corresponding authors upon reasonable request. Source data are provided with this paper.

References

1. Prat, I. et al. Observation of Fe(V)=O using variable-temperature mass Spectrometry and its enzyme-like C–H and C=C oxidation reactions. *Nat. Chem.* **3**, 788–793 (2011).
2. Onderko, E. et al. Characterization of a selenocysteine-ligated P450 compound I reveals direct link between electron donation and reactivity. *Nat. Chem.* **9**, 623–628 (2017).
3. Lancaster, K. M. Sizing up a dupercharged ferryl. *Proc. Natl. Acad. Sci. USA***115**, 4532–4534 (2018).
4. Van Heuvelen, K. M. et al. One-electron oxidation of an oxoiron(IV) complex to form an $[O=Fe^{V}=NR]^+$ center. *Proc. Natl. Acad. Sci. USA* **109**, 11933–11938 (2012).
5. Zhao, Y. et al. α-Fe_2O_3 as a versatile and efficient oxygen atom transfer catalyst in combination with H_2O as the oxygen source. *Nat. Catal.* **4**, 684–691 (2021).
6. Wang, Z. et al. Aqueous iron(IV)-oxo complex: an emerging powerful reactive oxidant formed by iron(II)-based advanced oxidation processes for oxidative water treatment. *Environ. Sci. Technol.* **56**, 1492–1509 (2022).
7. Sastri, C. V. et al. Axial ligand tuning of a nonheme iron(IV)-oxo unit for hydrogen atom Abstraction. *Proc. Natl. Acad. Sci. USA* **104**, 19181–19186 (2007).
8. Yokota, S. & Fujii, H. Critical factors in determining the heterolytic versus homolytic bond cleavage of terminal oxidants by Iron(III) porphyrin complexes. *J. Am. Chem. Soc.* **140**, 5127–5137 (2018).
9. McGarrigle, E. M. & Gilheany, D. G. Chromium- and manganese-salen promoted epoxidation of alkenes. *Chem. Rev.* **105**, 1563–1602 (2005).
10. Hirao, H., Li, F., Que, L. Jr. & Morokuma, K. Theoretical study of the mechanism of oxoiron(IV) formation from H_2O_2 and a nonheme Iron(II) complex: O-O cleavage involving proton-coupled electron transfer. *Inorg. Chem.* **50**, 6637–6648 (2011).
11. Li, M. et al. Highly selective synthesis of surface Fe^{IV}=O with nanoscale zero-valent iron and chlorite for efficient oxygen transfer reactions. *Proc. Natl. Acad. Sci. USA* **120**, e2304562120 (2023).
12. Baek, J. et al. Bioinspired metal-organic framework catalysts for selective methane oxidation to methanol. *J. Am. Chem. Soc.* **140**, 18208–18216 (2018).
13. Cheaib, K. et al. Selective formation of an $Fe^{IV}O$ or an $Fe^{III}OOH$ intermediate from Iron(II) and H_2O_2: controlled heterolytic versus homolytic oxygen-oxygen bond cleavage by the second coordination sphere. *Angew. Chem. Int. Ed.* **58**, 854–858 (2019).
14. Liang, S. et al. Fe^{2+}/HClO reaction produces $Fe^{IV}O^{2+}$: an enhanced advanced oxidation process. *Environ. Sci. Technol.* **54**, 6406–6414 (2020).
15. Kim, J. et al. Advanced oxidation process with peracetic acid and Fe(II) for contaminant degradation. *Environ. Sci. Technol.* **53**, 13312–13322 (2019).
16. Zhao, W. et al. Fe-O clusters anchored on nodes of metal-organic frameworks for direct methane oxidation. *Angew. Chem. Int. Ed.* **60**, 5811–5815 (2021).
17. Bernasconi, L., Louwerse, M. J. & Baerends, E. J. The role of equatorial and axial ligands in promoting the activity of non-heme oxidoiron(IV) catalysts in alkane hydroxylation. *Eur. J. Inorg. Chem.* **19**, 3023–3033 (2007).
18. Li, X. et al. CoN_1O_2 single-atom catalyst for efficient peroxymonosulfate activation and selective cobalt(IV)=O generation. *Angew. Chem. Int. Ed.* **62**, e202303267 (2023).
19. Li, X. et al. Breaking the symmetry of nitrogen-coordinated single-atom catalysts for advanced peroxymonosulfate oxidation. *ChemCatChem* **16**, e202301442 (2024).
20. Bell, N. et al. Uranyl to uranium(IV) conversion through manipulation of axial and equatorial ligands. *J. Am. Chem. Soc.* **140**, 3378–3384 (2018).
21. Ling, C. et al. Sulphur vacancy derived anaerobic hydroxyl radical generation at the pyrite-water interface: pollutants removal and pyrite self-oxidation behavior. *Appl. Catal. B: Environ.* **290**, 120051 (2021).
22. Ling, C. et al. Atomic-layered Cu_5 nanoclusters on FeS_2 with dual catalytic sites for efficient and selective H_2O_2 activation. *Angew. Chem. Int. Ed.* **61**, e202200670 (2022).
23. Ling, C. et al. Symmetry dependent activation and reactivity of peroxysulfates on FeS_2 (001). *Surf. Sci. Bull.* **69**, 154–158 (2024).
24. Hu, G. et al. Decomposition and oxidation of pyrite. *Prog. Energ. Combust.* **32**, 295–314 (2006).
25. Xu, Q. et al. Iron species activating chlorite: neglected selective oxidation for water treatment. *Environ. Sci. Ecotechnol.* **14**, 100225 (2023).
26. Su, R. et al. Revealing the generation of high-valent cobalt species and chlorine dioxide in the Co_3O_4-activated chlorite process:

insight into the proton enhancement effect. *Environ. Sci. Technol.* **57**, 1882–1893 (2023).
27. Dong, Z. et al. Study of pyrite oxidation with chlorine dioxide under mild conditions. *Miner. Eng.* **133**, 106–114 (2019).
28. Kim, H. H. et al. Activation of hydrogen peroxide by a titanium oxide-supported iron catalyst: evidence for surface Fe(IV) and its selectivity. *Environ. Sci. Technol.* **54**, 15424–15432 (2020).
29. Jo, Y. et al. Activation of peroxymonosulfate on visible light irradiated TiO_2 via a charge transfer complex path. *Chem. Eng. J.* **346**, 249–257 (2018).
30. Su, R. et al. Utilizing the oxygen-atom trapping effect of Co_3O_4 with oxygen vacancies to promote chlorite activation for water decontamination. *Proc. Natl. Acad. Sci. USA* **121**, e2319427121 (2024).
31. Zhang, Y. et al. Electronic delocalization regulates the occupancy and energy level of Co $3dz^2$ orbitals to enhance bifunctional oxygen catalytic activity. *Adv. Funct. Mater.* **32**, 2209499 (2022).
32. Choi, C. et al. The Achilles' heel of iron-based catalysts during oxygen reduction in an acidic medium. *Energy Environ. Sci.* **11**, 3176–3182 (2018).
33. Hou, K. et al. Reactive high-spin iron(IV)-oxo sites through dioxygen activation in a metal-organic framework. *Science* **382**, 547–553 (2023).
34. Zou, Y. et al. Tailoring the coordination environment of cobalt in a single-atom catalyst through phosphorus doping for enhanced activation of peroxymonosulfate and thus efficient degradation of sulfadiazine. *Appl. Catal. B: Environ.* **312**, 121408 (2022).
35. Li, Z. et al. Robust ring-opening reaction via asymmetrically coordinated Fe single atoms scaffolded by spoke-like mesoporous carbon nanospheres. *Proc. Natl. Acad. Sci. USA* **120**, e2218261120 (2023).
36. Huang, R. et al. Corrigendum to "three-dimensional porous high boron-nitrogen-doped carbon for the ultrasensitive electrochemical detection of trace heavy metals in food samples". *J. Hazard. Mater.* **456**, 131638 (2023).
37. Wu, C. et al. Orbital electron delocalization of axial-coordinated modified FeN_4 and structurally ordered PtFe intermetallic synergistically for efficient oxygen reduction reaction catalysis. *Chem. Sci.* **15**, 12989–13000 (2024).
38. Li, L. et al. Symmetry-broken steered delocalization state in a single-atom photocatalyst. *Nano Lett.* **24**, 14412–14419 (2024).
39. Liu, B. et al. Tailoring the selective generation of high-valent cobalt-oxo by asymmetrically coordinated single-atom cobalt-activated peracetic acid for efficient water decontamination. *Chem. Eng. J.* **499**, 156042 (2024).
40. Dummer, N. et al. Methane oxidation to methanol. *Chem. Rev.* **123**, 6359–6411 (2023).
41. Li, H. et al. Pt overlayer for direct oxidation of CH_4 to CH_3OH. *Chin. Chem. Lett.* **34**, 108292 (2023).
42. Yang, Z. et al. Partial oxidation of methane by photocatalysis. *Chin. Chem. Lett.* **35**, 108418 (2024).
43. Dinh, K. et al. Viewpoint on the partial oxidation of methane to methanol using Cu- and Fe-exchanged zeolites. *ACS Catal.* **8**, 8306–8313 (2018).
44. Hammond, C. et al. Direct catalytic conversion of methane to methanol in an aqueous medium by using copper-promoted Fe-ZSM-5. *Angew. Chem. Int. Ed.* **51**, 5129–5133 (2012).
45. An, B. et al. Direct photo-oxidation of methane to methanol over a mono-iron hydroxyl site. *Nat. Mater.* **21**, 932–938 (2022).
46. Tucci, F. J. & Rosenzweig, A. C. Direct methane oxidation by copper- and iron-dependent methane monooxygenases. *Chem. Rev.* **124**, 1288–1320 (2024).

Acknowledgements

This work was supported by the National Key Research and Development Program of China (2023YFC3708002, L.Z.), the Science and Technology special fund of Hainan Province (ZDYF2025SHFZ030, Y.Y.), the National Natural Science Foundation of China (U22A20402, L.Z. and 22476126, Y.Y.) and the Natural Science Foundation of Shanghai (22ZR1431700, Y.Y.). The authors acknowledge the support from the Instrumental Analysis Center of Shanghai Jiao Tong University and the Instrumental Analysis Center of the School of Environmental Science and Engineering, Shanghai Jiao Tong University.

Author contributions

L.Z., Y.Y., and W.L. conceived the idea and designed the experiments. L.Z. and Y.Y. supervised the project. W.L. performed the experiments. H.X. carried out the theoretical calculations. X.Z., M.L., C.L., and Y.S. provided experimental assistance. X.Z., J.D., M.L., C.L., Y.S., and H.L. participated in the discussion of the results during the manuscript preparation. L.Z., Y.Y., and W.L. wrote the paper.

Competing interests

The authors declare no competing interests.

Additional information

Supplementary information The online version contains supplementary material available at https://doi.org/10.1038/s41467-025-60919-7.

Correspondence and requests for materials should be addressed to Yancai Yao or Lizhi Zhang.

Peer review information *Nature Communications* thanks Wen Liu, Yuchao Zhang, and the other, anonymous, reviewer(s) for their contribution to the peer review of this work. A peer review file is available.